FERROMAGNETISM

# Fast fabrication of a hierarchical nanostructured multifunctional ferromagnet

Yingxin Hua[1]†, Xiaohong Li[1]†, Jiaxu Li[2], Xiang Luo[2], Yuqing Li[3], Wenyue Qin[1], Liqiang Zhang[1], Jianwei Xiao[4], Weixing Xia[5], Ping Song[1], Ming Yue[3], Hai-Tian Zhang[2]*, Xiangyi Zhang[1]*

Materials with multifunctionality affect society enormously. However, the inability to surmount multiple functionality trade-offs limits the discovery of next-generation multifunctional materials. Departing from conventional alloying design philosophy, we present a hierarchical nanostructure (HNS) strategy to simultaneously break multiple performance trade-offs in a material. Using a praseodymium-cobalt ($PrCo_5$) ferromagnet as a proof of concept, the resulting HNS outperforms contemporary high-temperature ferromagnets with a 50 to 138% increase in electrical resistivity while achieving their highest energy density. Our strategy also enables an exceptional thermal stability of coercivity (−0.148%/°C)—a key characteristic for device accuracy and reliability—surpassing that of existing commercial rare-earth magnets. The multifunctionality stems from the deliberately introduced nanohierarchical structure, which activates multiple micromechanisms to resist domain wall movement and electron transport, offering an advanced design concept for multifunctional materials.

Materials that combine different physical properties and functions are needed to meet rising global demands for saving energy, conserving resources, and improving human health (*1*–*7*). For example, anticancer drugs require materials with targeting and imaging capabilities (*4*), and implant materials need not only structural reliability but also biocompatibility (*5*). Similarly, artificial muscles in soft robots require simultaneous assurance of high energy efficiency and good flexibility (*6*). The need for multifunctionality becomes especially pronounced in sensing and actuating applications that consume >40% of global electricity (*2*, *7*), demanding a singular multifunctional material to fulfill pivotal criteria, such as efficiency, accuracy, reliability, and safety (*2*). Ferromagnetic materials are one example of materials that are crucial for these applications (*2*, *7*, *8*). High energy density, which requires both high saturation magnetization ($M_s$) and large coercivity ($H_c$) (*9*), is essential for maximizing energy efficiency (*7*, *8*). Large electrical resistivity is required to minimize eddy current loss and ensure safety (*2*) because the eddy current–related energy loss in motors is associated with the electrical resistivity of ferromagnets (*10*). Robust thermal stability, which is the ability against thermally driven magnetic instability, is necessary for achieving high accuracy and reliability. However, in a ferromagnetic material, the energy density and electrical resistivity are usually mutually exclusive and can only be enhanced at the expense of each other (*11*, *12*). Existing methods that enhance electrical resistivity introduce insulating and nonmagnetic components and thus reduce $M_s$, lowering the energy density (*9*). To hinder thermally driven magnetic instability, such as the decline of $H_c$, the conventional approach merely prioritizes the enhancement of $H_c$ itself (*13*, *14*) rather than addressing the material internal factors that cause the instability. This strategy inevitably introduces non- and weak-magnetic components or uses expensive heavy rare-earth elements (*7*, *13*), reducing the $M_s$ and thus the energy density. Moreover, a long-standing trade-off between the $M_s$ and $H_c$ exists (*9*, *13*, *15*–*17*), limiting the energy density that can be obtained. These trade-offs among essential physical properties create a fundamental dilemma for ferromagnetic materials to achieve the desired multifunctionality. Similarly, in other material systems, realizing multifunctionality has proven extremely challenging owing to the intricate trade-offs among various functionalities.

Conventional strategies relying on complex alloying designs often encounter a dilemma. Improving one aspect through the addition of alloying elements invariably compromises other important properties, substantially restricting material performance. For example, although traditional doping or alloying strategies have the potential to enhance the electronic properties of thermoelectric materials through electronic band engineering, they often adversely affect the thermal properties (*18*, *19*). Moreover, although the alloying strategy can result in improved mechanical properties for a magnetic material, it often comes at the cost of $M_s$ because of the introduction of nonmagnetic elements (*20*). Besides, the complex alloying design renders materials manufacturing complicated, costly, and wasteful of resources (*1*, *21*). The increased demand for alloying elements not only increases energy consumption during the production of the alloying metals but also leads to elevated $CO_2$ emissions (*1*), thereby exacerbating environmental concerns.

Deviating from the alloying design strategy, natural materials can well reconcile the conflicts among different properties by constructing hierarchical structures from nano- to micro- or macroscales with emerging mechanisms that give rise to multifunctionality (*22*, *23*). We hypothesize that similar principles could be applied to human-made materials to create the desired multifunctionality, through designing hierarchical nanostructures (HNSs) with rich and ordered substructures to synergistically manipulate magnetic, electrical, thermal, and optical properties. In contrast to traditional hierarchical materials that upscale from nano- and meso- to macroscales, our HNS features a distinctive hierarchical structure cascading from the nanoscale to the atomic scale with abundant interfacial effects and atomic-scale composition variations. Our nanohierarchical structure enables the effective manipulation of domain wall movement (*13*), electron and phonon transport (*18*, *24*), and light propagation (*25*), which underlie the aforementioned physical properties. Despite great advances in the synthesis of hierarchical structures (*3*, *26*), however, conventional methods have difficulty in producing an HNS owing to prolonged processing times and unregulated synthesis kinetics that inevitably lead to excessive grain growth and the loss of metastable substructures in the fabrication process. Constructing fully dense bulk HNSs with independently tailored nanoscale and atomic-scale features remains an even greater challenge. To craft such intricate bulk HNSs, a fast fabrication technique, especially at high temperatures, is imperative.

We developed a structural design strategy to simultaneously overcome multiple trade-offs in creating multifunctional materials by engineering HNSs. We used a ferromagnetic material as a proof of concept because it has complicated performance trade-offs, including the trade-off between energy density and electrical resistivity, the compromise between energy density and thermal stability, and the conflict between $M_s$ and $H_c$. All of these are essential factors to maximizing the energy efficiency, accuracy, reliability, and safety of devices (*2*, *7*). Our resulting HNS ferromagnet exhibits an attractive combination of multiple functional properties beyond existing high-temperature ferromagnets, with high energy density, large

[1]Center for Extreme Deformation Research, State Key Laboratory of Metastable Materials Science and Technology, Yanshan University, Qinhuangdao 066004, China. [2]School of Materials Science and Engineering, Beihang University, Beijing 100191, China. [3]Faculty of Materials and Manufacturing, Key Laboratory of Advanced Functional Materials, Ministry of Education of China, Beijing University of Technology, Beijing 100124, China. [4]Department of Materials Science and Engineering, City University of Hong Kong, Hong Kong, China. [5]CISRI & NIMTE Joint Innovation Center for Rare Earth Permanent Magnets, Ningbo Institute of Material Technology and Engineering, Chinese Academy of Sciences, Ningbo 315201, China.
*Corresponding author. Email: htzhang@buaa.edu.cn (H.-T.Z.); xyzh66@ysu.edu.cn (X.Z.)
†These authors contributed equally to this work.

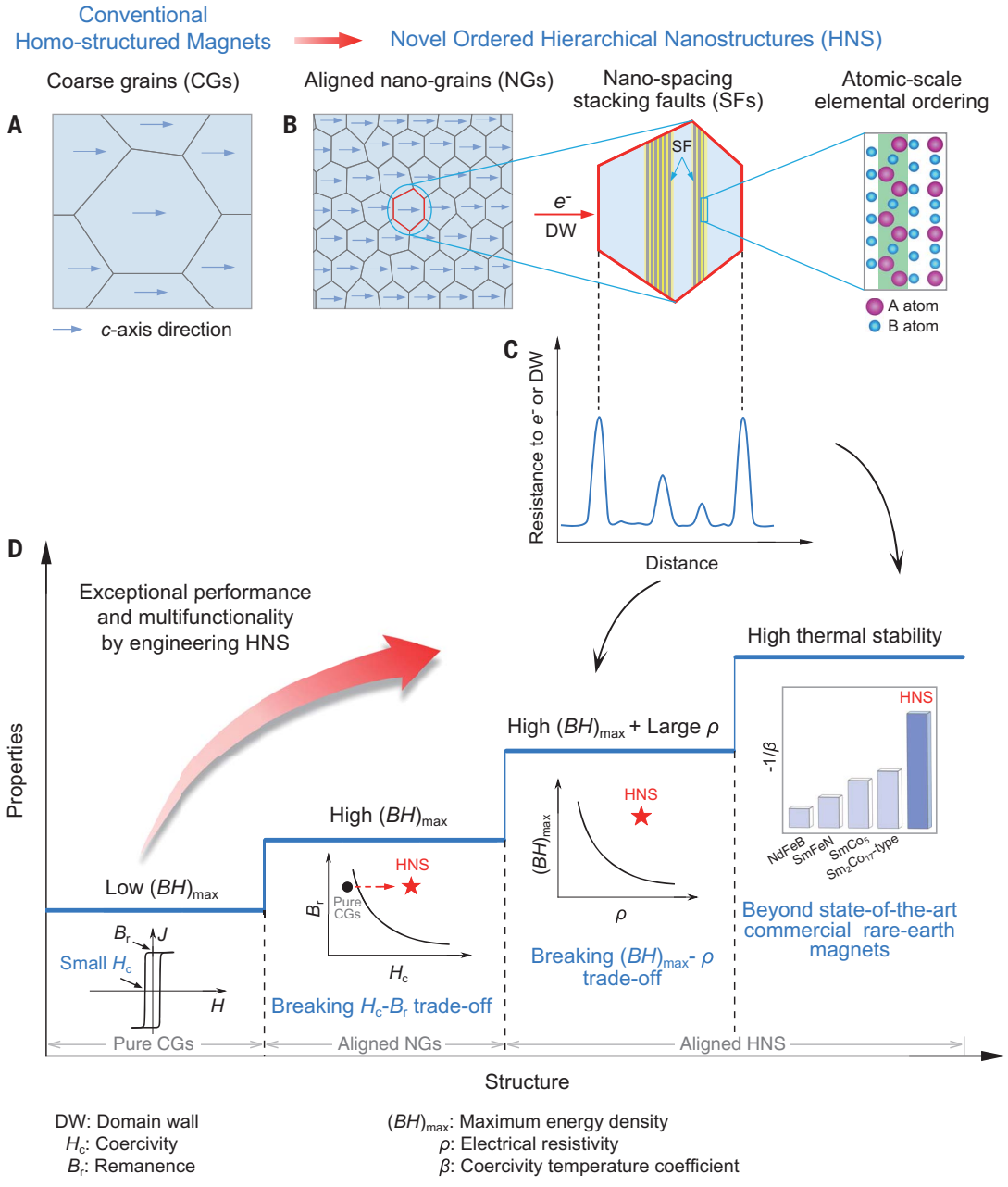


**Fig. 1. Concept of HNS to create multifunctional ferromagnetic materials.** (**A**) Schematic drawing of the microstructure of conventional permanent-magnet materials with a homogeneous CGS. (**B**) Schematic illustration of the design concept of HNS at multiple length scales. (**C**) Schematic of the enhanced resistance to domain wall (DW) movement and electron ($e^-$) transport in HNS materials. (**D**) Schematic representation of the impact of HNS on material properties. A pure CG material has a small coercivity ($H_c$) owing to large grain sizes and thus low energy density $(BH)_{max}$. The aligned nanograined (NG) material exhibits a large $H_c$ while maintaining high remanence ($B_r$), yielding high $(BH)_{max}$. The aligned HNS material enables a superior combination of high $(BH)_{max}$ and large electrical resistivity (ρ) as well as high thermal stability of $H_c$ that is represented by $-1/\beta$, where β is the temperature coefficient of $H_c$.

electrical resistivity, and excellent thermal stability of coercivity. Although our proof-of-concept report focuses on the simultaneous manipulation of domain wall movement and electron transport in the HNS through its abundant nanoscale interfacial effects and atomic-scale scattering, the underlying concept can be extended to construct other multifunctional materials, allowing simultaneous control over phonon transport and light propagation as well as the transport of reactants.

In contrast to conventional complex alloying design philosophy, our strategy takes a fundamentally distinct approach to develop multifunctional materials by focusing on the construction of nanoscale hierarchical structure (Fig. 1, A and B). This strategy can eliminate the necessity for numerous alloying elements and rely solely on a compositionally plain binary alloy, simplifying material fabrication and evading the trade-off dilemma from adding alloying elements. Furthermore, the Joule heating–based constrained deformation technique that we devised enables a rapid synthesis of fully dense, large-scale bulk materials in a matter of seconds to kinetically yield the HNS, providing a robust platform for the fabrication of intricate bulk HNS materials with tunable nanoscale and atomic-scale features.

Our HNS design concept is to create aligned nanograins embedded with high-density substructures, accompanied by atomic-scale local composition variations (Fig. 1B). This conceptual design enables us not only to substantially resist domain wall movement and electron transport with abundant interface effects and composition variations (Fig. 1C) to target high coercivity ($H_c$) and large electrical resistivity (ρ) but also to maintain high remanent magnetization ($B_r$) with aligned nanograins (along the easy magnetization axis—i.e., the $c$ axis) and the high $M_s$ of the compositionally plain alloys, achieving high energy density (Fig. 1D). Moreover, the engineered HNS also has a notable thermal stability of $H_c$ (Fig. 1D) owing to its enhanced resistance against the nucleation and growth of reverse domains.

### HNS construction and characterization

To validate this design concept, we chose a simple $PrCo_5$ binary alloy as a model system

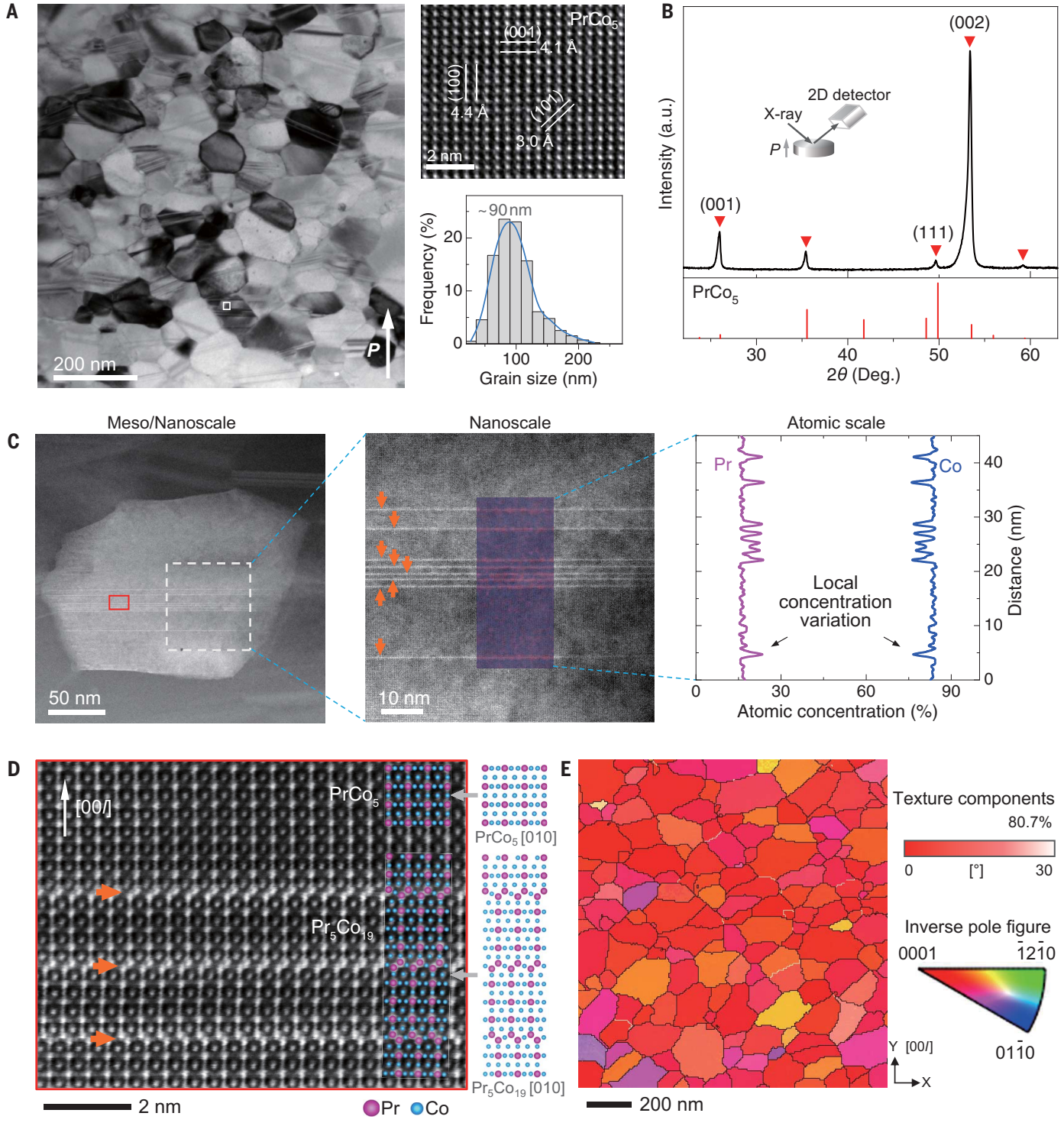


**Fig. 2. Microstructural characterization of the designed HNS materials.** (**A**) Typical bright-field TEM (left) and HRTEM (top right) images as well as the grain-size distribution histogram (bottom right) of the deformed sample ($T_d$ = 790°C) along the pressure direction. (**B**) XRD patterns of the sample measured perpendicular to the pressure direction (see the inset). The standard XRD patterns of the $PrCo_5$ compound are shown in the bottom part. a.u., arbitrary units; 2D, two-dimensional. (**C**) Spherical aberration–corrected STEM-HAADF images taken from the individual grain (left) and grain interior (middle) as well as atomic-scale line profile of EDS (right) yielded from the region marked in the HAADF image (middle), revealing an HNS across multiple length scales—i.e., the submicro- and nanoscale grains, nanospaced substructures, and atomic-scale composition variation within the grains. (**D**) An atomic-resolution STEM-HAADF image of the HNS material (left) and the schematics of the crystal structure of $PrCo_5$ [010] and $Pr_5Co_{19}$ [010] (right), revealing high-density SFs (indicated with red arrows) on the basal plane of the $PrCo_5$ matrix that yield localized $Pr_5Co_{19}$ phase. The HAADF image was taken from the region marked with the red square in the left panel of (C). (**E**) A typical TEBSD image (left) and texture components as well as the inverse pole figure (right) of the HNS material.

because it yields stacking faults (SFs) that can act as substructures and atomic-scale elemental ordering upon deformation based on our first-principles calculations (fig. S1), meeting our requirements for HNS. To create the desired HNS, we devised a Joule heating–based high-pressure constrained deformation technique (*27*) with amorphous precursors (fig. S2). This technique allows us to achieve high stress (up to gigapascals) and large strain and enables the rapid fabrication of fully dense materials in seconds, as compared with conventional magnet manufacturing methods that use polycrystalline materials and require hours to days of processing time for high-temperature sintering. In our method, the short processing times (in <20 s; fig. S3), along with high stress and large strain, enable the generation of PrCo nanograins with high-density SFs from the amorphous precursors at high temperatures (e.g., 790°C), and those with SFs perpendicular to the pressure direction have a low strain energy that facilitates grain-preferred growth and *c*-axis alignment, as SFs often form on the basal plane in hexagonal system materials because of a small SF energy (*28*). Using this approach, an HNS with aligned nanograins could be created in the PrCo binary alloys.

We first characterized the microstructure of deformed bulk samples with transmission electron microscopy (TEM) and x-ray diffraction (XRD) techniques, parallel and perpendicular to the pressure direction. We found that the deformed sample consists of approximately equiaxed grains with an average size of ~90 nm (Fig. 2A and fig. S4)—distinct from conventional hot-deformed magnets that typically have disc-shaped grains with large sizes up to micrometer scale—and that most grains contain a high density of substructures approximately perpendicular to the pressure direction (Fig. 2A and fig. S5), even across the whole grains (fig. S6). We identified the nanograins as $PrCo_5$ with high-resolution TEM (HRTEM) (Fig. 2A), which we confirmed by XRD analyses (Fig. 2B). The exclusively high (00*l*) diffraction peaks from the measurements perpendicular to the pressure direction indicate the *c*-axis alignment of most $PrCo_5$ grains along the pressure direction in the material, which is further confirmed by the XRD measurements parallel to the pressure direction, where the (00*l*) peaks completely disappear (fig. S7).

To characterize the substructures within the PrCo grains, we performed spherical aberration–corrected scanning transmission electron microscopy (STEM) analyses. The STEM high-angle annular dark-field (STEM-HAADF) images clearly reveal high-density parallel substructures (indicated with arrows) with nanoscale spacing down to ~1.6 nm within the $PrCo_5$ grains (Fig. 2C). We identified these substructures as SFs on the basal plane of $PrCo_5$ by atomic-resolution STEM-HAADF image analyses (Fig. 2D), which is supported by our first-principles calculations (fig. S1) that predict the formation of high-density SFs in $PrCo_5$ matrix upon severe deformation. Moreover, an atomic-scale line profile of energy dispersive spectrometer (EDS) reveals an ordered local atomic concentration (composition) variation—i.e., the richness of Pr atoms in the grains (Fig. 2C)—which is associated with the formation of SFs. This conclusion is directly confirmed by the atomic-resolution STEM-HAADF image of the SFs (Fig. 2D), where Pr atoms replace partial Co atoms at the SFs, which reduces SF energy according to our theoretical calculations (fig. S1). We also characterized the alignment degree of $PrCo_5$ grains in the material with a transmission electron backscatter diffraction (TEBSD) technique, revealing a strong [00*l*] texture with >80% of grains being aligned (Fig. 2E). These results suggest that an ordered HNS material composed of aligned $PrCo_5$ nanograins embedded with high-density SFs, along with atomic-scale local composition variations, has been fabricated with our approach. Further studies show that the HNS characteristics, such as grain size, SF density, and alignment degree, can be controllably modulated with processing parameters (fig. S8).

## Multifunctional properties

We next determined whether the HNS materials that we synthesized exhibit the desired multifunctionality with good magnetic and electrical properties as well as high thermal stability. For a comparative study, we deliberately prepared an HNS material with smaller nanograins (HNS-S) and a material with a conventional coarse-grained structure (CGS) without the hierarchy (fig. S9). The CGS $PrCo_5$ shows a small intrinsic coercivity ($H_{ci}$) of ~3 kOe (Fig. 3A), similar to that of conventional $PrCo_5$ sintered magnets (Fig. 3, B and C) (*29*–*35*). As expected, the HNS $PrCo_5$ exhibits a high $H_{ci}$ of 7.3 kOe, more than two times as large as that of the CGS material without sacrificing the remanence $B_r$. This result suggests that the long-standing $H_{ci}$-$B_r$ trade-off has been broken by engineering the HNS with aligned nanograins. We obtained a higher $H_{ci}$ = 10.5 kOe, more than triple that of the CGS material, in the HNS-S material with a smaller average grain size of ~50 nm (fig. S9). Consequently, the HNS materials exhibit an attractive combination of high $H_{ci}$ and high $B_r$ beyond that of previously reported $PrCo_5$ magnets (Fig. 3B), yielding a high energy product $(BH)_{max}$ = 33 megagauss-oersted (MGOe) for the $PrCo_5$ magnets that typically have values below 25 MGOe (Fig. 3C). The energy product that we achieved is 83% higher than that of the CGS (18 MGOe), 38 to 65% larger than that of $SmCo_5$ high-temperature magnets (20 to 24 MGOe) (*8*, *13*), and even reaches the highest values (30 to 33 MGOe) of state-of-the-art $Sm_2(Co,Fe,Cu,Zr)_{17}$ high-temperature commercial magnets (*8*, *13*), yet with plain alloy composition that enables a high $M_s$ (12.2 kG).

The HNS $PrCo_5$ also exhibits a large electrical resistivity ρ up to 105 microhm•cm at ambient temperature (table S1). This value exceeds those of the $SmCo_5$ [ρ = 44 microhm•cm (*36*)] and $Sm_2(Co,Fe,Cu,Zr)_{17}$ [ρ = 70 microhm•cm (*37*)] magnets with 50 to 138% enhancement and is also 75% larger than that of the CGS $PrCo_5$ (ρ = 60 microhm•cm) (table S1). We refer to the $Sm_2(Co,Fe,Cu,Zr)_{17}$ magnet as a $Sm_2Co_{17}$-type magnet. To highlight the superior combination of the $(BH)_{max}$ and ρ in the HNS and HNS-S $PrCo_5$, we compared them with the representative $SmCo_5$ and $Sm_2Co_{17}$-type commercial magnets, the CGS $PrCo_5$, and $SmCo_5$ hybrid composites in a $(BH)_{max}$–ρ plot (Fig. 3D) (*13*, *37*–*39*). The HNS $PrCo_5$ exhibits an exceptional combination of high $(BH)_{max}$ and large ρ, beyond those of conventional $SmCo_5$ and $Sm_2Co_{17}$-type high-temperature commercial magnets, outperforming the $SmCo_5$ magnets with more than double ρ and a 38 to 65% increase in $(BH)_{max}$ and improving over the $Sm_2Co_{17}$-type magnets by a 50% increase in ρ while achieving their highest $(BH)_{max}$ (Fig. 3D). This superior combination also surpasses that of the CGS $PrCo_5$ with an 83% increase in $(BH)_{max}$ and a 75% enhancement in ρ (Fig. 3D). Similarly, the HNS-S $PrCo_5$ exhibits a good combination of the high $(BH)_{max}$ and large ρ in Fig. 3D. Furthermore, our HNS materials show an excellent thermal stability of $H_{ci}$, which is indicated by −1/β with an extremely small temperature coefficient of β = −0.148%/°C for the HNS-S $PrCo_5$ and β = −0.171%/°C for the HNS $PrCo_5$ (Fig. 3E), surpassing that of the CGS $PrCo_5$ (−0.205%/°C) and those of existing commercial rare-earth magnets, including NdFeB (−0.611%/°C), SmFeN (−0.4%/°C), $SmCo_5$ (−0.255%/°C), and $Sm_2Co_{17}$-type (−0.227%/°C) magnets (*7*, *40*). This high thermal stability enables the HNS-S material to maintain a large $H_{ci}$ at 400°C similar to that of the $Sm_2Co_{17}$-type magnets (Fig. 3F). The exceptional thermal stability of $H_{ci}$ in both the HNS and HNS-S $PrCo_5$ might stem from a small temperature degradation of the anisotropy field of the $PrCo_5$ alloy (*41*) and an enhanced resistance to the nucleation and growth of reverse domains because nanograins enable both the high-density grain boundaries (GBs) to resist domain wall movement and the small stray fields to resist reverse domain nucleation (*42*). Consequently, despite their mutually conflicting attributes, a synergetic enhancement of the $M_s$, $H_{ci}$, $(BH)_{max}$, ρ, and −1/β (the thermal stability of $H_{ci}$) has been realized by engineering the HNS with aligned nanograins as compared with both the CGS $PrCo_5$ and conventional SmCo commercial magnets, which demonstrates the superiority of the HNS strategy in enhancing the properties of ferromagnetic materials and creating multifunctionality. By contrast, although bonded magnets can achieve a high ρ, the $(BH)_{max}$ is

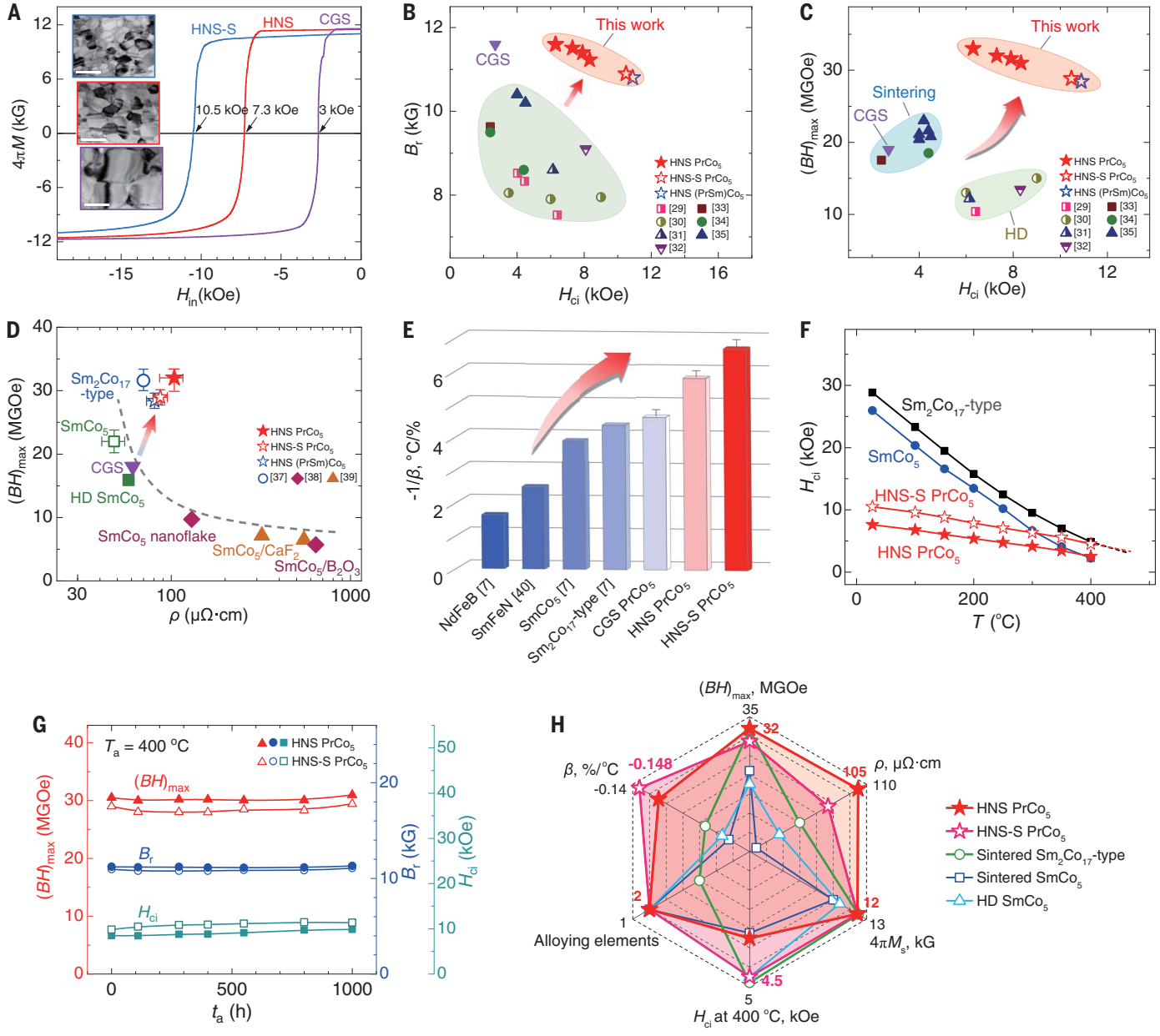


**Fig. 3. Magnetic and electrical properties of the new HNS materials.** (**A**) Typical demagnetization curves of the HNS-S, HNS, and CGS $PrCo_5$ measured along the pressure direction at ambient temperature. The insets show their bright-field TEM images (scale bars, 200 nm). (**B**) Comparison of the $B_r$ and $H_{ci}$ of the HNS materials, CGS $PrCo_5$, and representative $PrCo_5$ magnets. (**C**) Plot of $(BH)_{max}$–$H_{ci}$ of the HNS materials, CGS $PrCo_5$, and representative $PrCo_5$ sintered and hot-deformed (HD) magnets. (**D**) Comparison of the $(BH)_{max}$ and ρ of the HNS materials, CGS $PrCo_5$, representative $SmCo_5$ and $Sm_2Co_{17}$-type high-temperature magnets, and $SmCo_5$ hybrid composites. Ω, ohm. (**E**) Comparison of the thermal stability of $H_{ci}$ of the HNS materials, CGS $PrCo_5$, and existing commercial rare-earth magnets. The thermal stability is characterized with the parameter of $-1/\beta$ (where β is the temperature coefficient of $H_{ci}$). The representative commercial rare-earth magnets include Nd-Fe-B (*7*), Sm-Fe-N (*40*), $SmCo_5$ (*7*), and $Sm_2(Co,Fe,Cu,Zr)_{17}$ (*7*) materials. (**F**) Temperature dependence of the $H_{ci}$ for the HNS materials and commercial $SmCo_5$ and $Sm_2Co_{17}$-type magnets. (**G**) Long-term thermal stability assessment of magnetic properties of the HNS materials after annealing at $T_a$ = 400°C for various times $t_a$. (**H**) Comprehensive comparison of the properties of the HNS materials in contrast to SmCo-based high-temperature permanent-magnet materials, including commercial sintered $SmCo_5$ and $Sm_2Co_{17}$-type magnets, as well as HD $SmCo_5$ magnets. An inverse scale is used for both the β and alloying elements (i.e., the number of alloying elements).

substantially reduced to about one-eighth or half of the conventional oriented magnets for isotropic and oriented bonded magnets (*13*), respectively, due to the presence of high-volume nonmagnetic binders. Such a big $(BH)_{max}$–ρ trade-off limits their application in motors. Moreover, the temperature sensitivity of the binders is another critical obstacle for the application of bonded magnets in motors (*7*).

To reveal the underlying mechanism of the unusual combination of high energy product and large electrical resistivity in the HNS material, we first performed in situ Lorentz TEM observations of its magnetization reversal under applied magnetic fields (Fig. 4, A to C, and movie S1). We found two kinds of domain wall pinning sites, one in the grain interior under small applied fields (Fig. 4B)

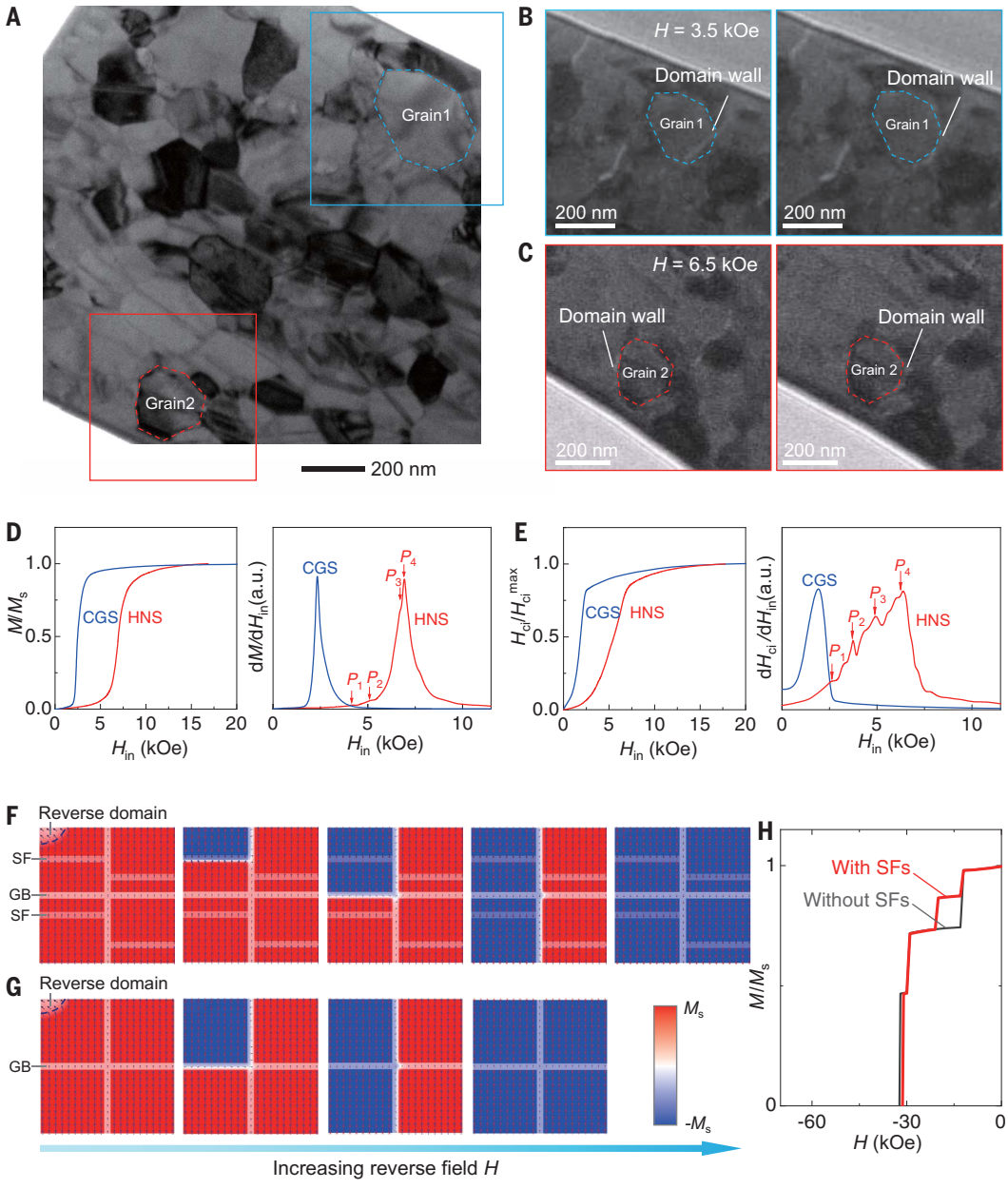


**Fig. 4. Magnetization reversal of the HNS $PrCo_5$ materials.** (**A**) Bright-field TEM image of the HNS specimen. (**B**) In situ Lorentz TEM images before (left) and after (right) domain wall movement in the region marked with the blue square in (A), revealing domain wall pinning in the grain interior (grain 1) under a small applied field ($H$ = 3.5 kOe). (**C**) In situ Lorentz TEM images before (left) and after (right) domain wall movement in the region marked with the red square in (A), revealing domain wall pinning at GB (grain 2) under a large applied field ($H$ = 6.5 kOe). (**D**) Initial magnetization curves (left) and their corresponding differential curves (right) of the CGS and HNS $PrCo_5$. (**E**) Applied field dependence of $H_{ci}$ (left) and their corresponding differential curves (right) of the CGS and HNS $PrCo_5$. The HNS material exhibits a multistep pinning behavior, as indicated with multiple pinning sites [(D) and (E), right panels] and a large distribution of switching fields, fundamentally distinct from the CGS material. (**F** and **G**) Micromagnetism simulations of the magnetization reversal process of the HNS and the material without SFs. For the HNS, the reverse domain is first pinned at the SF under the reverse magnetic field, then depinning occurs with increasing the reverse field, and the domain wall is subsequently pined at the GB. The GB pinning controls the $H_{ci}$ of the HNS material. (**H**) Micromagnetism-simulated demagnetization curves of the $PrCo_5$ materials with and without SFs in grains.

and the other at GBs under large applied fields (Fig. 4C). The former can be rationally attributed to the high-density SFs within the grains. The atomic-scale local composition variations could also cause domain wall energy variations that pin domain walls (*43*). We confirmed the multistep pinning behavior by analyzing both the initial magnetization curve (Fig. 4D) and the applied-field dependence of $H_{ci}$ (Fig. 4E), which show the existence of multiple pinning sites (indicated with arrows) in the HNS material. We reproduced these behaviors by micromagnetism simulations of the magnetization reversal of the HNS (Fig. 4F), showing domain wall pinning sequentially at the SF and the GB. The latter determines the $H_{ci}$, which agrees with our in situ Lorentz TEM observations under large applied fields, where the domain wall pinning occurs almost exclusively at the GBs (movie S2). Our findings suggest that the activation of multiple micromechanisms against domain wall movement effectively impedes magnetization reversal in the HNS material, which enables high $H_{ci}$ and large squareness $S$ in demagnetization curve without sacrificing $M_s$, yielding high energy product. A large $S$ is found in the demagnetization curve of the HNS by micromagnetism simulations of the materials with and without SFs (Fig. 4, F and G)—$S$ = 0.85 for $PrCo_5$ grains with SFs and 0.81 for the ones without SFs (Fig. 4H).

The large ρ that we observed could also stem from the activation of multiple micromechanisms to scatter electrons in the HNS materials. The ρ in a material is given as (*44*)

$$\rho = \frac{m_e^*}{e^2 n \tau} \quad (1)$$

where $m_e^*$ is the effective mass of the electron in a crystal, $e$ is the electron charge, $n$ is the electron concentration, and τ is the mean scattering time of electrons that is directly related to the microscopic processes that cause the scattering of the electrons in the material, including lattice vibrations, crystal imperfections, and impurities (*44*). In the HNS materials, high-density GBs and nanospaced SFs, as well as

atomic-scale composition variations that cause lattice distortion, can substantially enhance the mean frequency of electron scattering events ($1/\tau$), yielding a large ρ. This conclusion is supported by a plot of ρ–grain size ($d$) for the material (fig. S10). The smaller the $d$, the larger the ρ. The data that deviate from the linear relationship indicate the contribution of high-density mutually parallel SFs (fig. S8) to electron scattering in the material. Our result is supported by our theoretic calculations (*27*) that yield a large ρ—double that of $PrCo_5$—for $Pr_5Co_{19}$ that contains high-density SFs in the $PrCo_5$ matrix.

To further reveal the mechanism of the large ρ in the HNS $PrCo_5$, we performed finite element simulations of the impact of SF fraction on the ρ (*27*). We found the ρ increases linearly with the SF fraction (fig. S11), which agrees with the previously established theoretical model that indicates a linear increase of ρ with SF density (*45*). These results suggest that the electron scattering caused by SFs also contributes to the enhancement of ρ in the HNS materials.

Our HNS materials exhibit good thermal stability. We did not observe degradation in magnetic properties, such as $(BH)_{max}$, $B_r$, and $H_{ci}$, after 1000 hours of annealing at 400°C (Fig. 3G). We also found no clear change in the microstructure (fig. S12). The slight increase in $H_{ci}$ with annealing time might stem from the change of interfacial chemistry and structure of the HNS materials. With the spherical aberration–corrected STEM-HAADF technique, we identified the change of interfacial chemistry from an enrichment of ferromagnetic element Co into a Pr enrichment in the HNS $PrCo_5$ after annealing (fig. S13). We suggest that such interfacial chemistry change could weaken the magnetic exchange coupling between the $PrCo_5$ nanograins and increase the magnetocrystalline anisotropy at interfaces (*13*), thus increasing the $H_{ci}$ (*46*). After 400°C annealing (fig. S14), we did not find any obvious decrease in electrical resistivity. The periodic arrangement of SFs within the $PrCo_5$ matrix constituted a localized metastable $Pr_5Co_{19}$ phase (Fig. 2D) that could exist below 417°C (*47*).

To highlight the excellent combination of multiple properties of our HNS materials, we compared them with representative SmCo high-temperature permanent-magnet materials (Fig. 3H). The HNS and HNS-S $PrCo_5$ alloys exhibit an exceptional combination of high $(BH)_{max}$, large ρ, high $-1/\beta$, and high $M_s$, along with less alloying elements, outperforming the prevailing $Sm_2Co_{17}$-type high-temperature magnets. The HNS-S $PrCo_5$ also has a large $H_{ci}$ (at 400°C), similar to that of the $Sm_2Co_{17}$-type magnet. A smaller β of −0.131%/°C and a larger $H_{ci}$ of 12 kOe could be expected by decreasing their grain size down to 20 nm (fig. S15), and the magnetic properties can also be tailored with Sm addition to yield even larger $H_{ci}$ (fig. S16). The extremely high $-1/\beta$, coupled with a high Curie temperature of $T_c$ = 630°C (fig. S17), makes the HNS $PrCo_5$ materials appropriate for high-temperature applications. More importantly, the compositionally plain alloy design not only enables high $M_s$ but also minimizes the reliance on alloying elements. This strategy is entirely different from current prevailing magnet manufacturing practices that require compositionally complex alloying design. Furthermore, our manufacturing process with the fast fabrication speed (in <20 s) and the utilization of amorphous precursors (*27*) starkly contrasts with that of existing high-temperature magnets. This is especially true for the $Sm_2Co_{17}$-type magnets, which begin with polycrystalline precursors and require days of slow sintering process and complex heat treatments at high temperatures (850° to 1200°C) (*7*), which poses energy and emission concerns as well as low production rate.

Although the quantity of materials processed in a single run with our method is smaller compared with conventional sintering technology, we suggest that the rapid fabrication speed of our method could enable a certain scale of production of permanent magnets through enhancing the production rate. Our technology can produce the HNS magnets with multifunctional characteristics that were previously out of reach. These features are crucial for high-value niche applications, such as in aerospace sensors and actuators as well as in medical devices that have very stringent performance requirements. Our strategy is general and can be extended to other permanent magnetic materials, such as $SmCo_5$ and $(Sm,Pr)Co_5$ (fig. S18 and Fig. 3, B to D).

## Conclusions

Departing from the conventional alloying design strategy, we demonstrate an HNS design concept for overcoming multiple trade-offs in creating multifunctional materials through the emerging physical mechanisms induced by the HNS, where diverse functional mechanisms are activated through the abundant interfacial effects of the nanohierarchical structure. Our HNS strategy leads to the discovery of a class of multifunctional high-temperature ferromagnetic materials with an exceptional combination of high energy product, large electrical resistivity, and superior thermal stability of coercivity—surpassing that of existing high-temperature ferromagnets. This achievement breaks a long-standing dilemma that essential properties of ferromagnetic materials can only be enhanced at the expense of each other. The unusual combination of high energy density and large electrical resistivity in the HNS ferromagnet leads to a reduction in eddy current loss from 161.1 W/kg to 72.1 W/kg and a working temperature drop of ~27°C in drive motors as compared with its conventional counterpart (fig. S19), which is further demonstrated by our experimental results (fig. S20), contributing to enhanced efficiency and safety in electric cars. Moreover, the simultaneous possession of excellent thermal stability of coercivity opens up potential applications in special sensors, circulators, and actuators. All of these devices demand high accuracy and reliability.

Although this is a proof-of-concept study that focuses on the simultaneous manipulation of domain wall movement and electron transport by engineering HNSs, we believe that the fundamental concept can be extended to simultaneously control phonon transport and light propagation as well as the transport of reactants. This should make our strategy generally applicable to other material systems to yield desirable multifunctionality, including ferroelectric, thermoelectric, and catalytic materials, where multiple conflicting properties need to be overcome (*48*). Furthermore, our Joule heating–based constrained deformation technology provides a rapid fabrication platform for creating bulk HNS materials with tunable nanoscale and atomic-scale features and facilitating the discovery of next-generation multifunctional materials for technological applications. We also anticipate the potential applications of this fast, far-from-equilibrium fabrication technique to generate a diverse array of high-performance materials, featuring various metastable structures and metastable phases that remain beyond the reach of conventional methods.

## REFERENCES AND NOTES


1. D. Raabe, C. C. Tasan, E. A. Olivetti, *Nature* **575**, 64–74 (2019).
2. J. M. Silveyra, E. Ferrara, D. L. Huber, T. C. Monson, *Science* **362**, eaao0195 (2018).
3. D. Nepal *et al*., *Nat. Mater.* **22**, 18–35 (2023).
4. Z. Cheng, A. Al Zaki, J. Z. Hui, V. R. Muzykantov, A. Tsourkas, *Science* **338**, 903–910 (2012).
5. C. Li *et al*., *Nat. Rev. Mater.* **5**, 61–81 (2020).
6. X. Qian, X. Chen, L. Zhu, Q. M. Zhang, *Science* **380**, eadg0902 (2023).
7. O. Gutfleisch *et al*., *Adv. Mater.* **23**, 821–842 (2011).
8. N. Jones, *Nature* **472**, 22–23 (2011).
9. D. J. Sellmyer, *Nature* **420**, 374–375 (2002).
10. D. Ishak, Z. Q. Zhu, D. Howe, *IEEE Trans. Magn.* **41**, 2462–2469 (2005).
11. Z. H. Kautsar *et al*., *J. Alloys Compd.* **942**, 168855 (2023).
12. J. He *et al*., *J. Mater. Sci. Technol.* **154**, 54–64 (2023).
13. J. M. D. Coey, *Engineering* **6**, 119–131 (2020).
14. J. Li *et al*., *Acta Mater.* **161**, 171–181 (2018).
15. X. Li *et al*., *Adv. Mater.* **29**, 1606430 (2017).
16. L. Lou *et al*., *Adv. Mater.* **33**, e2102800 (2021).
17. B. Balasubramanian, B. Das, R. Skomski, W. Y. Zhang, D. J. Sellmyer, *Adv. Mater.* **25**, 6090–6093 (2013).
18. G. J. Snyder, E. S. Toberer, *Nat. Mater.* **7**, 105–114 (2008).
19. S. Roychowdhury *et al*., *Science* **371**, 722–727 (2021).
20. L. Han *et al*., *Nature* **608**, 310–316 (2022).
21. X. Li, K. Lu, *Science* **364**, 733–734 (2019).
22. M. A. Meyers, J. McKittrick, P.-Y. Chen, *Science* **339**, 773–779 (2013).
23. R. O. Ritchie, *Nat. Mater.* **10**, 817–822 (2011).
24. K. Biswas *et al*., *Nature* **489**, 414–418 (2012).
25. A. M. Shaltout, V. M. Shalaev, M. L. Brongersma, *Science* **364**, eaat3100 (2019).
26. R. Liang *et al*., *Nat. Mater.* **21**, 1434–1440 (2022).

27. Materials and methods are available as supplementary materials online.
28. C. He *et al*., *Acta Mater.* **188**, 328–343 (2020).
29. D. Zhang *et al*., *RSC Adv.* **5**, 90976–90982 (2015).
30. A. M. Gabay, W. F. Li, G. C. Hadjipanayis, *J. Magn. Magn. Mater.* **323**, 2470–2473 (2011).
31. W. Q. Liu *et al*., *J. Appl. Phys.* **109**, 07A731 (2011).
32. A. M. Gabay, Y. Zhang, G. C. Hadjipanayis, *J. Magn. Magn. Mater.* **294**, 287–293 (2005).
33. Y. Shen, D. Laughlin, E. Velu, S. Sankar, *J. Magn. Magn. Mater.* **94**, 57–66 (1991).
34. E. Velu, R. Obermyer, S. Sankar, W. Wallace, *J. Less Common Met.* **148**, 67–71 (1989).
35. W. Wallace *et al*., *Mater. Sci. Forum* **30**, 177–186 (1988).
36. S. Ruoho, M. Haavisto, E. Takala, T. Santa-Nokki, M. Paju, *IEEE Trans. Magn.* **46**, 15–20 (2010).
37. O. Gutfleisch, M. Verdier, I. R. Harris, A. Ray, *IEEE Trans. Magn.* **29**, 2872–2874 (1993).
38. A. M. Gabay, M. Marinescu-Jasinski, W. F. Li, J. F. Liu, G. C. Hadjipanayis, *J. Appl. Phys.* **109**, 07A719 (2011).
39. A. M. Gabay, M. Marinescu-Jasinski, C. N. Chinnasamy, J. F. Liu, G. C. Hadjipanayis, *J. Magn. Magn. Mater.* **324**, 2879–2884 (2012).
40. M. Matsuura *et al*., *J. Magn. Magn. Mater.* **467**, 64–68 (2018).
41. A. S. Ermolenko, *IEEE Trans. Magn.* **12**, 992–996 (1976).
42. H. Sepehri-Amin, T. Ohkubo, M. Gruber, T. Schrefl, K. Hono, *Scr. Mater.* **89**, 29–32 (2014).
43. A. Yan, O. Gutfleisch, T. Gemming, K. H. Müller, *Appl. Phys. Lett.* **83**, 2208–2210 (2003).
44. S. O. Kasap, *Principles of Electronic Materials and Devices* (McGraw-Hill, ed. 3, 2006), pp. 117–127.
45. A. Howie, *Philos. Mag.* **5**, 251–271 (1960).
46. H. Sepehri-Amin *et al*., *Acta Mater.* **126**, 1–10 (2017).
47. A. E. Ray, K. J. Strnat, *IEEE Trans. Magn.* **11**, 1429–1430 (1975).
48. X. Zhang, *Mater. Res. Lett.* **8**, 49–59 (2020).

## ACKNOWLEDGMENTS

We thank M. Li, J. Z. Chen, and F. C. Hou for their help in deformation and spherical aberration–corrected STEM experiments. **Funding:** This work was financially supported by the National Natural Science Foundation of China (grant no. 51931007, X.Z. and M.Y.; grant no. U22A20116, X.Li and H.-T.Z.; grant no. 52071279, X.Li; and grant no. 52271236, H.-T.Z.); the National Key R&D Program of China (grant no. 2022YFB3505600, H.-T.Z.); and the Science Research Project of Hebei Education Department (JZX2024022, L.Z.). **Author contributions:** X.Z. led the project. X.Z. and H.-T.Z. conceived the concept of ordered HNS. X.Z., H.-T.Z., and X.Li designed and conducted the experiments. Y.H., W.Q., and P.S. produced and investigated the HNS materials. Y.H. and W.Q. carried out microstructural characterization and magnetic measurements. H.-T.Z. and J.L. performed the measurements of electrical property and the finite element simulations of electrical resistivity. H.-T.Z. and X.Lu. carried out ANSYS Motor-CAD simulation analysis. H.-T.Z., J.L., and X.Lu. measured the magnet temperature rise under alternating magnetic field. L.Z. carried out spherical aberration–corrected STEM experiments and STEM-HAADF analyses. W.X. conducted Lorentz TEM observations. Y.L. and M.Y. performed micromagnetism simulations. J.X. carried out the theoretical calculations of SF energy and electrical resistivity. All authors discussed the results. X.Z., H.-T.Z., X.Li, and Y.H. wrote the paper. **Competing interests:** All authors declare no competing interests. **Data and materials availability:** All data are available in the main text or the supplementary materials. 

## SUPPLEMENTARY MATERIALS

science.org/doi/10.1126/science.adp2328
Materials and Methods
Supplementary Text
Figs. S1 to S22
Tables S1 and S2
References (*49*–*58*)
Movies S1 and S2

Submitted 14 March 2024; accepted 26 June 2024
10.1126/science.adp2328